Monthly Notices
of the
ROYAL ASTRONOMICAL SOCIETY

MNRAS **452,** 1902–1913 (2015) doi:10.1093/mnras/stv1410

Near-infrared polarimetric adaptive optics observations of NGC 1068: a torus created by a hydromagnetic outflow wind

E. Lopez-Rodriguez,[1★†] C. Packham,[1] T. J. Jones,[2] R. Nikutta,[3] L. McMaster,[1] R. E. Mason,[4] M. Elvis,[5] D. Shenoy,[2] A. Alonso-Herrero,[6‡] E. Ramírez,[7] O. González Martín,[8,9,10] S. F. Hönig,[11] N. A. Levenson,[12] C. Ramos Almeida[9,10§] and E. Perlman[13]

[1]*Department of Physics & Astronomy, University of Texas at San Antonio, One UTSA Circle, San Antonio, TX 78249, USA*
[2]*Minnesota Institute for Astrophysics, University of Minnesota, 116 Church Street SE, Minneapolis, MN 55455, USA*
[3]*Instituto de Astrofísica, Facultad de Física, Pontificia Universidad Católica de Chile, 306, Santiago 22, Chile*
[4]*Gemini Observatory, Northern Operations Center, 670 N. A'ohoku Place, Hilo, HI 96720, USA*
[5]*Harvard–Smithsonian Center for Astrophysics, 60 Garden St, Cambridge, MA 02138, USA*
[6]*Instituto de Física de Cantabria, CSIC-UC, E-39005 Santander, Spain*
[7]*IAG, Universidade de São Paulo, Rua do Matão 1226, Cidade Universitária, São Paulo 05508-900, Brazil*
[8]*Centro de Radioastronomía y Astrofísica (CRyA-UNAM), 3-72 (Xangari), 8701 Morelia, Mexico*
[9]*Instituto de Astrofísica de Canarias, Calle Vía Láctea s/n, E-38205 Tenerife, Spain*
[10]*Departamento de Astrofísica, Universidad de La Laguna, E-38206 La Laguna, Tenerife, Spain*
[11]*Dark Cosmology Center, Niels Bohr Institute, University of Copenhagen, Juliane Maries Vej 30, DK-2100 Copenhagen, Denmark*
[12]*Gemini Observatory, Casilla 603, La Serena, Chile*
[13]*Department of Physics and Space Sciences, Florida Institute of Technology, Melbourne, FL 32901, USA*

Accepted 2015 June 23. Received 2015 June 9; in original form 2015 February 11

ABSTRACT

We present J' and K' imaging linear polarimetric adaptive optics observations of NGC 1068 using MMT-Pol on the 6.5-m MMT. These observations allow us to study the torus from a magnetohydrodynamical (MHD) framework. In a 0.5 arcsec (30 pc) aperture at K', we find that polarization arising from the passage of radiation from the inner edge of the torus through magnetically aligned dust grains in the clumps is the dominant polarization mechanism, with an intrinsic polarization of 7.0 ± 2.2 per cent. This result yields a torus magnetic field strength in the range of 4–82 mG through paramagnetic alignment, and 139^{+11}_{-20} mG through the Chandrasekhar–Fermi method. The measured position angle (P.A.) of polarization at K' is found to be similar to the P.A. of the obscuring dusty component at few parsec scales using infrared interferometric techniques. We show that the constant component of the magnetic field is responsible for the alignment of the dust grains, and aligned with the torus axis on to the plane of the sky. Adopting this magnetic field configuration and the physical conditions of the clumps in the MHD outflow wind model, we estimate a mass outflow rate $\leq$0.17 $M_\odot$ yr^{-1} at 0.4 pc from the central engine for those clumps showing near-infrared dichroism. The models used were able to create the torus in a time-scale of $\geq 10^5$ yr with a rotational velocity of $\leq$1228 km s^{-1} at 0.4 pc. We conclude that the evolution, morphology and kinematics of the torus in NGC 1068 can be explained within a MHD framework.

Key words: magnetic fields – MHD – polarization – instrumentation: adaptive optics – techniques: high angular resolution.

1 INTRODUCTION

The torus is the cornerstone of the unified model (Lawrence 1991; Antonucci 1993; Urry & Padovani 1995) of Active Galactic Nuclei (AGNs). Specifically, this model posits that the observational differences between radio-quiet AGNs arise from an orientation effect. In this scheme, the AGN classification solely depends on

★E-mail: enrique.lopezrodriguez@utsa.edu
†Researcher Affiliated-Postdoctoral, Department of Astronomy, University of Texas at Austin.
‡Visiting Professor, Department of Physics and Astronomy, University of Texas at San Antonio.
§Marie Curie Fellow.

the anisotropic obscuration of the central engine (black hole and accretion disc) by an optically and geometrically thick, dusty torus. Although the torus was postulated to be a 'donut-shape' morphology, in this paper the term 'torus' is used to denote the region surrounding the central engine where the obscuring material is located, with the precise morphology of that region still to be determined.

Several ideas to explain the existence of the torus have been proposed. Some models explained the torus as an inflow of gas from few tens of kpc. Wada, Papadopoulos & Spaans (2009) presented numerical simulations of the interstellar medium to track the formation of molecular hydrogen forming an inhomogeneous thick disc around the central engine, identified as the torus. In a further 3D hydrodynamic simulation model, Wada (2012) found that a vertical circulation of gas in the central parsecs drives the formation of an obscuring region along the equatorial plane. Schartmann, Krause & Burkert (2011) suggested the origin of the torus as dusty clouds falling from the host galaxy to the central engine. Conversely, some models (Blandford & Payne 1982; Krolik & Begelman 1988; Emmering, Blandford & Shlosman 1992; Konigl & Kartje 1994; Kartje, Konigl & Elitzur 1999; Elitzur & Shlosman 2006) assume an outflowing wind confined and accelerated by the magnetic field generated in the accretion disc. In this scheme, the hydromagnetic wind can lift the plasma from the mid-plane of the accretion disc to form a geometrically thick distribution of dusty clouds surrounding the central engine. High angular resolution observations suggest the infrared (IR) emitting regions of the torus to no more than a few parsecs in radius (i.e. Radomski et al. 2003; Jaffe et al. 2004; Packham et al. 2005; Mason et al. 2006; Radomski et al. 2008; Raban et al. 2009; Ramos Almeida et al. 2009; Alonso-Herrero et al. 2011; Ramos Almeida et al. 2011; Burtscher et al. 2013; Ichikawa et al. 2015; Markowitz, Krumpe & Nikutta 2014). Within these scales, the torus is in the region where the supermassive black hole and accretion disc activity dominate over the galaxy components. Thus, the torus origin is likely influenced by the central engine, which gives strong impetus to the outflowing wind model.

Although large efforts have been made in the development of (magneto)hydrodynamical (MHD) simulations of the outflow wind of AGNs, the magnetic field strengths in the torus are poorly constrained. The magnetic field can induce a preferential orientation of dust grains within the torus that can give rise to a measurable degree of polarization (e.g. Davis & Greenstein 1951; Jones & Spitzer 1967; Jones, Klebe & Dickey 1992), with an expected linear degree of polarization <15 per cent at near-IR (NIR: 1–5 μm) assuming standard disc models (Efstathiou, McCall & Hough 1997). Hence, IR polarimetric techniques give us a powerful tool to enhance the contrast of the polarized structures arising from aligned dust grains, helping us to constrain the magnetic fields, from those unpolarized components within the core of AGNs. Using *J, H* and K_n imaging polarimetric observations on the 3.9-m Anglo-Australian Telescope, Lopez-Rodriguez et al. (2013) estimated a magnetic field strength in the range of 12–128 mG in the NIR emitting regions in the torus of IC 5063. Through comparison with the magnetic field strength of ∼2 mG estimated by the ratio of thermal and magnetic field pressure, they suggested that a magnetically dominant region is surrounding the central engine of IC 5063. They concluded that the magnetic field plays an important role in the torus evolution of IC 5063, favouring the MHD outflow wind model.

NGC 1068 is an archetypal type 2 AGN, whose proximity (we adopt $H_0 = 73\,\mathrm{km\,s^{-1}\,kpc^{-1}}$, thus 1 arcsec = 60 pc) and high brightness make it an ideal target for polarimetry. The detection of polarized broad emission lines in the optical (0.35–0.70 μm) wavelengths of NGC 1068 by Antonucci & Miller (1985) was crucial to understand the AGN structure. Their detection is most readily interpreted through scattering of the radiation from the central engine into our line of sight (LOS) by the ionization cones. After correction for starlight dilution, the continuum polarization was shown to be constant, ∼16 per cent, over the ultraviolet (Antonucci, Hurt & Miller 1994) and optical wavelengths (Miller & Antonucci 1993), with electron scattering being the dominant polarization mechanism. Further optical (0.5–0.6 μm) polarimetric studies (Capetti et al. 1995) using the *Hubble Space Telescope* (*HST*) showed a centrosymmetric polarization pattern along the ionization cones in the ∼10 arcsec (600 pc) central region. This polarization pattern is the signature of a central point source whose radiation (which can be polarized from multiple scattering into the funnel of the torus and/or broad line clouds) is ultimately polarized through scattering by dust and/or electrons. At ultraviolet and optical wavelengths, these studies showed that electron scattering is the dominant polarization mechanism in the core and ionization cones of NGC 1068. In the NIR, an increase in the polarization flux density with increasing wavelength in the core was observed (e.g. Lebofsky, Kemp & Rieke 1978; Brindle et al. 1990). Further modelling using NIR polarimetric observations has shown that the polarization in the core most likely arises from dichroic absorption of radiation from the central engine by aligned dust grains in the torus (Young et al. 1995; Packham et al. 1997; Lumsden et al. 1999; Simpson et al. 2002; Watanabe et al. 2003). A combination of electron and dust scattering from the ionization cones still has some contribution, i.e. <10 per cent of the polarized flux at 2.0 μm (Young et al. 1995). Hönig, Prieto & Beckert (2008) estimated that the contribution of the accretion disc emission to the total flux is negligible at 2.0 μm, and that dust emission from a clumpy torus is the dominant contributor. In addition, Watanabe et al. (2003) raise the possibility that scattering off large grains in the torus could also explain the NIR polarization. They argued that the change of position angle (P.A.) of polarization and the increase in the degree of polarization from optical to NIR due to dust scattering by large grains in the torus cannot be ruled out. Although detailed studies have not been done yet, some implications are discussed in Section 4.2.

In this paper, we examine the MHD outflow wind model in the core of NGC 1068 assuming the torus to be CLUMPY (Nenkova, Ivezic & Elitzur 2002; Nenkova et al. 2008a,b). We follow the approach from Lopez-Rodriguez et al. (2013) to estimate the magnetic field strength in the torus of NGC 1068 and extent the study to estimate physical parameters of the torus using MHD outflow wind models, allowing us to describe the evolution and kinematics of the clumps. We performed imaging polarimetric observations in the J' and K' filters using MMT-Pol in conjunction with the adaptive optics (AO) system on the 6.5-m MMT. The paper is organized as follows: Section 2 describes the observations and data reduction, Section 3 presents our polarimetric results, which are analysed in Section 4. In Section 5, we estimate the magnetic field strength in the torus of NGC 1068. Section 6 presents the discussion and Section 7 the conclusions.

2 OBSERVATIONS AND DATA REDUCTION

NGC 1068 was observed on 2013 October 23 using MMT-Pol (Packham & Jones 2008; Packham et al. 2010a,b) in conjunction with the AO system and the f/15 camera on the 6.5-m MMT, Arizona. The AO system was used to assist the polarimetric observations of MMT-Pol. Specifically, a dichroic at 15° to the normal before the aperture window of MMT-Pol reflects optical light up to a CCD-based wavefront sensor and passes the IR beam

Table 1. Summary of observations.

Object	Filter	Frame time (s)	# ABA	Total time (s)
NGC 1068	J'	15	3	540
	K'	10	10	1200
HD 38563C	J'	10	2	240
	K'	10	3	360

into MMT-Pol at the Cassegrain focus. Thus, NGC 1068 is used for the AO correction at optical wavelengths. MMT-Pol uses a 1024 × 1024 pixels HgCdTe AR-coated Virgo array, with a pixel scale of 0.043 arcsec pixel^{-1}, corresponding to a field of view (FOV) of 44 arcsec × 44 arcsec. MMT-Pol uses a rectangular focal plane aperture, a half-wave retarder (half wave plate, HWP), and one of two Wollaston prisms. The rectangular focal plane aperture provides two non-overlapping rectangular images with an individual FOV of 20 arcsec × 40 arcsec. In standard polarimetric observations, the HWP is rotated to four P.A. in the following sequence: 0°, 45°, 22.5 and 67.5. A Calcite Wollaston is used in the wavelength range of 1–2 μm and a Rutile Wollaston is used in the wavelength range of 2–5 μm.

The J' ($\lambda_c = 1.33$ μm, $\Delta\lambda = 0.08$ μm, 50 per cent cut-on/off) and K' ($\lambda_c = 2.20$ μm, $\Delta\lambda = 0.11$ μm, 50 per cent cut-on/off) filters provide the best combination of sensitivity and wavelength range within the instrumental filter set; thus, these filters were used for the observations. In both filters, the images were acquired in an ABA dither pattern with an offset of 8 arcsec in declination, where four HWP P.A. were taken in each dither position. The position of the short axis of the array with the north on the sky was 149° and 46° E of N at J' and K', respectively. At J', frame exposure times of 15 s per HWP P.A. at each dither position were taken, with a total of three ABA dither patterns, providing a total exposure time of 540 s. At K', frame exposure times of 10 s per HWP at each dither position were taken, with a total of 10 ABA dither patterns, providing a total exposure of 1200 s. A summary of observations is shown in Table 1.

The data were reduced using custom IDL routines and standard NIR imaging procedures. The difference for each correlated double sample pair was calculated, and then sky subtracted using the closest dither position in time to create a single image per HWP P.A. For each dither position, the ordinary (o-ray) and extraordinary (e-ray) rays, produced by the Wollaston prism, were extracted and then the Stokes parameters, I, Q and U were estimated according to the ratio method (e.g. Tinbergen 2006) for each dither position. The Stokes parameters were registered and shifted to a common position, and then co-averaged to obtain the final I, Q and U images. Finally, the degree, $P = \sqrt{Q^2 + U^2}/I$, and P.A., P.A. $= 0.5 \arctan(U/Q)$, of polarization were estimated. During this process, individual photometric and polarimetric measurements were performed for each dither position, allowing to examine for a high and/or variable background that could indicate the presence of clouds or electronic problems. Fortunately, no data needed to be removed for these reasons, but some data were removed when the AO guide unlocked. The measurements of the degree of polarization were corrected for polarization bias using the approach by Wardle & Kronberg (1974).

The image of the unpolarized standard star, HD 224467, in the K' filter was used to estimate the image quality of the observations, ensuring the quality of the AO system prior the science observations. For the standard star, the full width at half-maximum (FWHM) using a Gaussian profile was estimated to be 0.17 arcsec × 0.23 arcsec in the K' filter (Fig. 1, bottom-middle). MMT-Pol has a residual astigmatism that produces an X-shape on the FWHM. The polarized standard star, HD 38563C, was observed in both filters. The observations were performed during windy conditions on the observatory. The unpolarized standard star, HD 224467, was observed against the wind, minimizing instrumental shakes, whilst NGC 1068 observations were performed in favour of the wind, which affect the image quality. Frame exposure times of 10 s per HWP P.A. at each dither position were taken, with a total of two and three ABA dither patterns, providing a total exposure time of 240 and 360 s in the J' and K' filters, respectively. A summary of the observations is shown in Table 1. The observations show HD 38563C as an elongation due to the nebulae that the star is embedded. Although the FWHM of the observations were affected, the polarimetric measurements are not affected as these measurements were estimated in a large circular aperture assuming HD 38563C as a single source. In polarimetry, HD 38563C allows us to estimate the zero-angle calibration of the observations. The zero-angle calibration, $\Delta\theta$, was estimated as the difference of the measured P.A. of polarization of our observations, $\theta_{J'} = 25° \pm 5°$ and $\theta_{K'} = 37° \pm 2°$, and the P.A. of polarization, $\theta_J^W = 71° \pm 1°$ and $\theta_K^W = 78° \pm 17°$ provided by Whittet et al. (1992). Thus, the zero-angle calibrations were estimated to be $\Delta\theta_{J'} = \theta_J^W - \theta_{J'} = 46° \pm 5°$ and $\Delta\theta_{K'} = \theta_K^W - \theta_{K'} = 41° \pm 17°$. The instrumental polarization was measured to be 0.05 per cent ± 0.03 per cent using several unpolarized standard stars from Whittet et al. (1992) during the observing run.

3 RESULTS

Fig. 1 shows the J' (top-left) and K' (bottom-left) total flux images of NGC 1068. The extension towards the west in the K' total intensity image (Fig. 1-black diamond) is a ghost which we attribute to faint, internal reflections within the optics. This faint ghost does not appear in polarized intensity. The radial profiles of the total flux images at J' (top-right) and K' (bottom-right) of NGC 1068 and the unpolarized standard star, HD 224467, at K' are shown. The FWHMs in the longest and shortest direction and associated P.A., using a 2D Gaussian profile, were estimated to be 1.23 arcsec × 1.01 arcsec at P.A. = 56° E of N, and 0.48 arcsec × 0.38 arcsec at P.A. = 50° E of N in the J' and K' filters, respectively. Note that the FWHMs in Fig. 1 are calculated using the radial profiles. The estimated FWHM of NGC 1068 differs from those (∼0.12 arcsec at 2.2 μm) previously reported in the literature using high-spatial resolution observations (e.g. Rouan et al. 1998, 2004; Gratadour et al. 2006). Although the FWHM of NGC 1068 was affected during the observations, only those observations with (1) photometric conditions; (2) locked AO in a complete ABA and (3) good image quality, were used. Specifically, as the nucleus of NGC 1068 is faint, the AO system was forced to sample the optical image to lower frequencies compared to a bright star. At these lower frequencies, the AO system compensate less for seeing, exacerbated by the wind buffeting. To account for the impact of the weather condition and low AO camera frame rate in the measured flux, we estimated the variation of the counts between the several ABA's to be 12 per cent. This result is included in the uncertainties of the AGN flux contribution in Section 4.1.

Fig. 2 shows the polarized flux image and polarization vectors through the K' filter. The overlaid polarization vectors are proportional in length to the degree of polarization with their orientation showing the P.A. of polarization. To improve the signal-to-noise ratio (S/N) and to obtain statistically independent polarization measurements, the normalized Stokes parameters $q = Q/I$ and $u = U/I$

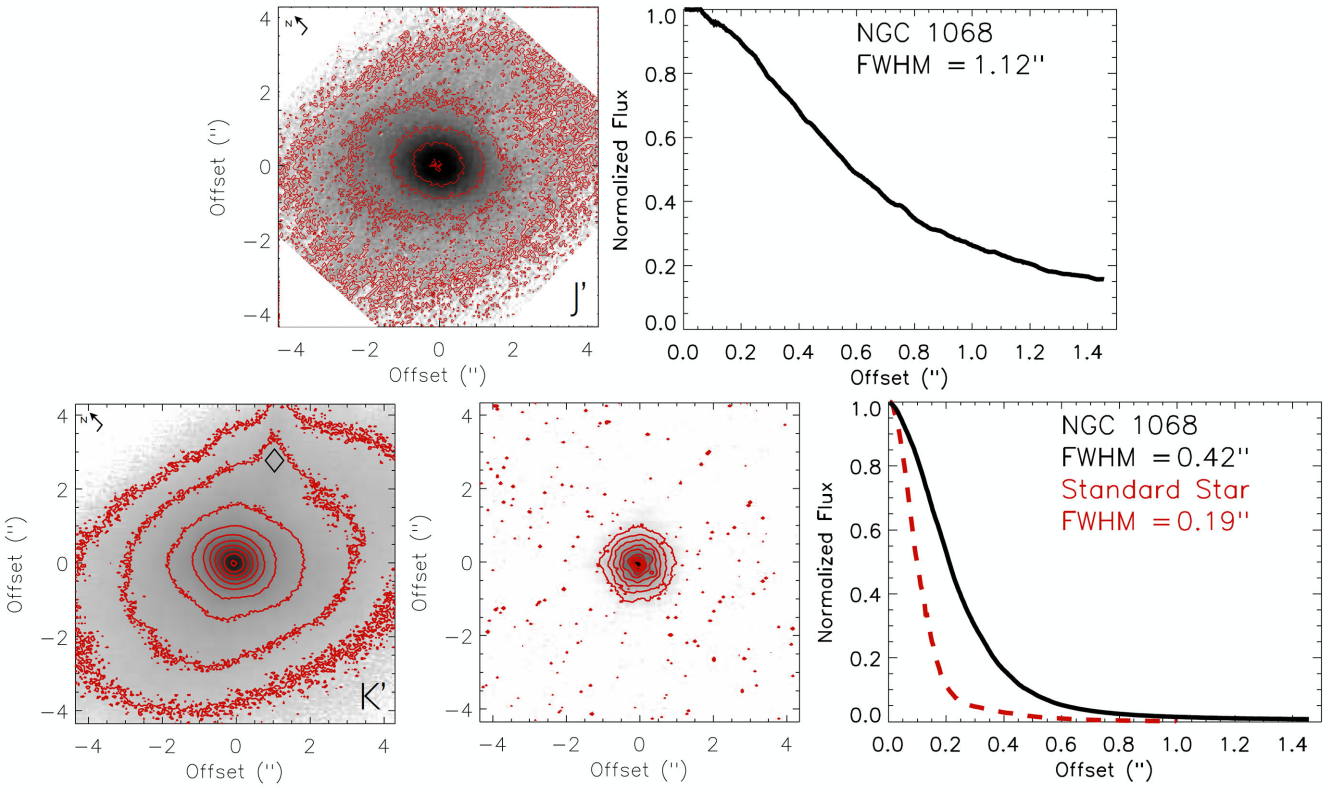

Figure 1. The 8.5 arcsec × 8.5 arcsec central region of NGC 1068 in the J' (first row) and K' (second row) total flux (grey-scale) images. In both images, the lowest level contour is at 8σ, then contours are at the sigma-levels of 2^n, where $n = 4$, 5, 6, etc. The J' image was rotated for direct comparison with K' image (Section 2). The ghost (black diamond) in the K' is marked. The middle plot of the second row shows the unpolarized standard star, HD 224467, at K' with the same FOV and contour levels as the total flux images of NGC 1068. In all the total flux images, the pixel scale is 0.043 arcsec pixel^{-1}. The radial profiles of NGC 1068 (black solid line) and the standard star (red dashed line), normalized to the flux density value of the centroid of NGC 1068, are shown.

were binned from 4×4 pixels (0.172 arcsec × 0.172 arcsec) to a single pixel. Then, only those polarization vectors with $P/\sigma_p > 3$ are shown in Fig. 2. σ_p is the uncertainty on the degree of polarization within the binned pixels, estimated as $\sigma_p = \sqrt{\sigma_u^2 + \sigma_q^2}$, where σ_q and σ_u are the uncertainties on the normalized Stokes parameters. In polarized flux, NGC 1068 shows a resolved nucleus with a FWHM estimated to be 0.49 arcsec × 0.45 arcsec at P.A. = 30° E of N. The polarization vectors and polarized flux image in the J' filter are not shown because of the low S/N ∼ 40 at the peak pixel of the observations.

To compare with previously published values (Table 2), we made measurements of the nuclear polarization at J' and K' in several apertures. In all cases, polarimetric errors were estimated by variation of the measurements in subsets of the data. Our measured polarization values in a 2 arcsec aperture are in close agreement with previously published values (Table 2). Simpson et al. (2002) measured a degree of polarization of 6.0 ± 1.2 per cent, with variations of ± 2–3 per cent in the degree of polarization between the two observing runs of NGC 1068, however the reason of this difference is unknown. We subsequently conclude that the measured polarization of Simpson et al. (2002) and ours, 4.8 ± 0.1 per cent, are in marginal agreement within the uncertainties. We found an increase in the degree of polarization with increasing wavelength, as expected from previous polarimetric studies (e.g. Lebofsky et al. 1978; Brindle et al. 1990; Young et al. 1995; Packham et al. 1997; Lumsden et al. 1999) with a roughly constant P.A. of polarization in the NIR wavelength.

We also made measurements of the nuclear polarization at J' and K' in a 0.5 arcsec (30 pc) aperture. These measurements minimize contamination from extended (diffuse) dust emission, as well as obtain a statistically independent measurement with higher S/N than the single polarization vectors (important in the J' filter due to the low S/N of the observations). Specifically, its degree of polarization was measured to be 2.9 ± 1.3 per cent and 4.4 ± 0.1 per cent with a P.A. of polarization of 111° ± 14° and 127° ± 2° in a 0.5 arcsec (30 pc) aperture in the J' and K' filters, respectively. The statistical significance of the degree of polarization measurements is 2.4σ and 36σ in the J' and K' filters, respectively.

The polarized flux image at K' shows a centrosymmetric polarization pattern (south-west lobe in Fig. 2) at ∼1.5 arcsec south from the centre of the galaxy. The degree of polarization is 15 ± 2 per cent within the binned 4 × 4 pixels (0.172 arcsec × 0.172 arcsec). This polarization pattern is the signature of a central source whose radiation is scattered by dust/electrons. This polarized structure and measured polarization are in excellent agreement with (1) the 2.0 μm polarimetric observations using *HST*/NICMOS by Simpson et al. (2002), and (2) the ionization cones, with opening angle of 65° ± 20° and P.A. ∼ 15°, observed using *HST* [O III] observations by Evans et al. (1991). We found a ∼49° misalignment between the measured P.A. of polarization at K' and the radio jet axis (Fig. 2, insert plot). This misalignment is similar to the ∼45° misalignment between the compact (1.35 × 0.45 pc) hot (∼800 K) dust component (i.e. obscuring torus) observed by Raban et al. (2009) and the radio jet axis. A further interpretation of this

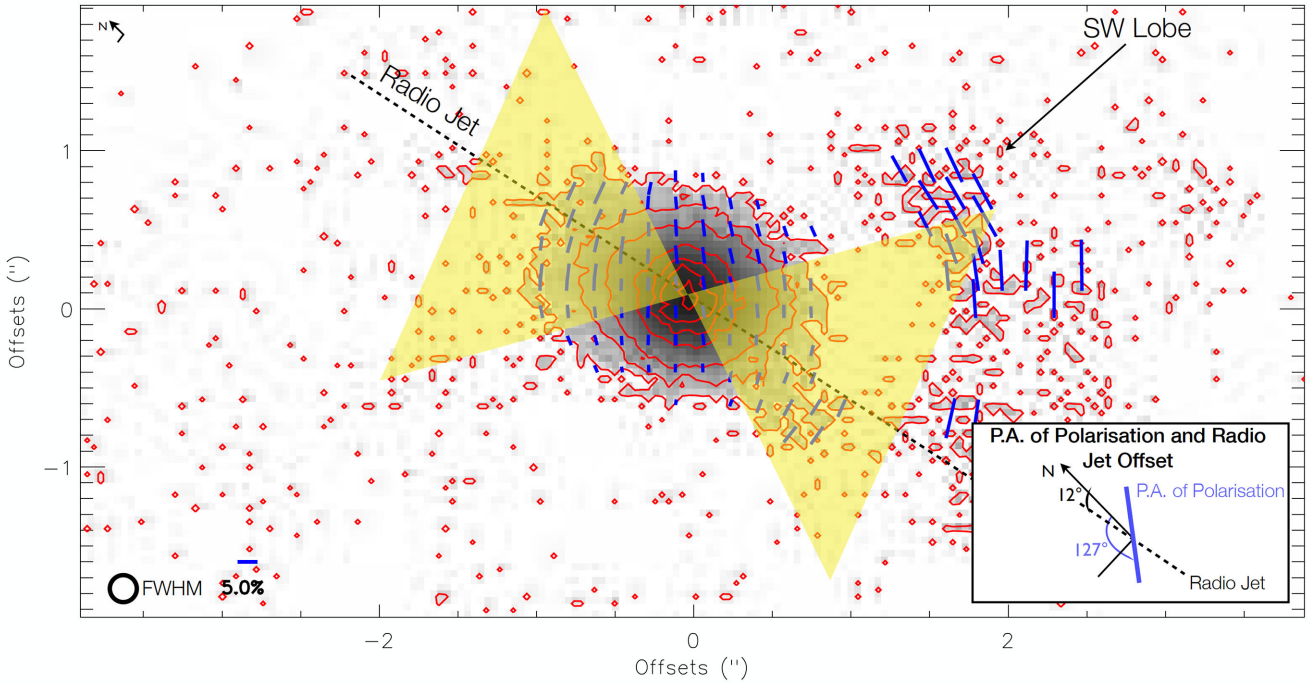

Figure 2. The 8 arcsec × 4 arcsec polarized flux image (grey-scale) at K' with overlaid polarization vectors. The contour levels are 1.5, 5, 10, 30, 50, 70 and 90 per cent of the peak of the polarized flux image. The polarized flux image has a pixel scale of 0.043 arcsec, whilst the polarization vectors with $P/\sigma_p > 3$ within the binned 4×4 pixels box (0.172 arcsec) are shown. A vector of 5 per cent of polarization and the FWHM of the observations are shown. The dashed line shows the orientation of the radio jet at P.A.∼ 12° by Gallimore et al. (1996), and the yellow shadow area shows the *HST* [O III] opening angle, 65° ± 20° with P.A.∼15°, by Evans et al. (1991). The P.A. of polarization and the radio jet axes (insert plot) with respect to the north is shown (Section 3).

Table 2. Nuclear polarimetry of NGC 1068 and literature values.

Aperture (arcsec)	Filter	P (per cent)	$P.A.$ (°)	Ref(s).
0.2	2.0 μm	6.0 ± 1.2	122 ± 15	a
	K'	4.8 ± 0.1	127 ± 2	b
0.5	J'	2.9 ± 1.3	111 ± 14	b
	K'	4.4 ± 0.1	127 ± 2	b
2.0	J	2.25 ± 0.25	106.8 ± 2.0	c
	J	1.71 ± 0.22	106.45 ± 1.70	d
	J'	2.4 ± 1.2	106 ± 17	b
	K_n	4.57 ± 0.50	120.2 ± 2.0	c
	K_n	4.11 ± 0.46	120.55 ± 2.38	d
	K'	4.2 ± 0.3	119 ± 5	b

References: (a) Simpson et al. (2002); (b) This work; (c) Lumsden et al. (1999); (d) Packham et al. (1997).

misalignment in terms of the MHD outflow wind model in AGN is given in Section 6.1.

4 ANALYSIS

4.1 AGN contribution to the total flux density

The emission from the unresolved core of NGC 1068 at K' can arise from two components: (1) diffuse stellar emission in the nuclear bulge, and (2) AGN emission. We interpret the AGN emission as a point-source emission component, while the diffuse stellar emission is extended. Photometric cuts through the nucleus in the J' filter show negligible evidence of a nuclear point-source, AGN emission, due to extinction towards the core and/or contamination by the diffuse stellar emission (Fig. 1, top-right). The J' filter profile is assumed to be representative of the diffuse stellar emission in the nuclear bulge. At K', both the AGN emission and diffuse stellar emission are detectable. To estimate the relative contributions from both emission components in the K' filter, two different methodologies were followed.

In the first method (method 1), we followed similar analysis to that of Turner et al. (1992), Packham et al. (1996) and Lopez-Rodriguez et al. (2013). We took photometric profiles along the major axis of the diffuse extended stellar emission in the J' and K' filters, which is shown to have a constant extinction of $A_V = 0.7 \pm 0.7$ (Young et al. 1995). These cuts allow us to characterize the host galaxy contribution. The contribution of the AGN emission is assumed to be the point spread function (PSF) of the observations (i.e. the unpolarized standard star, HD 224467). To fit the K'-profile, the emission was modelled as the sum of a scaled-PSF and the diffuse stellar emission from the J'-profile. Using this method the best estimate of AGN contribution to the total flux is 60 ± 12 per cent in a 0.5 arcsec (30 pc) aperture. The uncertainty was estimated as the 12 per cent uncertainty due to weather conditions and low AO camera frame rate (Section 3).

In the second method (method 2), the PSF from method 1 was scaled to the flux density of the K' emission to subtract the AGN emission. This procedure produces a 'flat-top' profile over the unresolved core of NGC 1068 (for examples of the use of this technique, see Radomski et al. 2002, 2003; Ramos Almeida et al. 2011; Lopez-Rodriguez et al. 2013). Using this method, the contribution of the AGN emission to the total flux is 50 ± 19 per cent in a 0.5 arcsec (30 pc) aperture. The uncertainty was estimated as the addition in quadrature of the uncertainty of the 'flat-top' method applied, 15 per cent, and the 12 per cent uncertainty due to weather conditions and low AO camera frame rate (Section 3).

From both methods presented above, the average of the AGN emission to the total flux is estimated to be 55 ± 16 per cent, whereas the contribution of the diffuse stellar emission to the total flux is 45 ± 16 per cent, in a 0.5 arcsec (30 pc) aperture in the K' filter. The formal total uncertainties are 16 per cent through the average of both methods. Systemic errors of methodologies could increase these estimates, but are difficult to quantify. For NGC 1068, Weinberger, Neugebauer & Matthews (1999) estimated the AGN contribution to be 49 ± 8 per cent of the total nuclear flux in a 0.48 arcsec aperture in the K filter using the near-infrared camera on the 10-m Keck I telescope. Weigelt et al. (2004) estimated a total flux contribution of 46 ± 5 per cent at K' in a 18 × 39 mas using NIR speckle interferometry on the 6-m Special Astrophysics Observatory.

4.2 The nuclear intrinsic polarization

The diffuse stellar emission in the nuclear regions of NGC 1068 significantly dilutes the observed polarization from the AGN. If only the dilution from the diffuse stellar emission is subtracted from the observed polarization, the estimated intrinsic polarization is independent of the dominant polarization mechanism in the nuclear regions of NGC 1068. Thus, the dominant polarization mechanism in the K' filter is needed to estimate the intrinsic degree of polarization of the AGN. The intrinsic degree of polarization arising from the dominant mechanism of polarization in the nuclear regions of NGC 1068 is estimated as follows. The measured polarization at K', $P^{\rm obs}_{K'} = 4.4 \pm 0.1$ per cent, in a 0.5 arcsec (30 pc) aperture is corrected by accounting for (1) the measured degree of polarization through dichroic absorption of starlight in an off-nuclear region ($P^{\rm off}_{K'}$), (2) the diffuse stellar emission relative to the AGN emission in the nuclear aperture ($R_{K'}$), and (3) the dominant polarization mechanism to the polarized flux of the AGN in the nuclear aperture ($F^{\rm dic}_{K'}$).

The degree of polarization at K' through dichroic absorption of starlight in the off-nuclear regions of NGC 1068 was measured to be $P^{\rm off}_{K'} = 0.5 \pm 0.3$ per cent. The off-nuclear polarization was estimated as the average of several polarization measurements using a 2 arcsec aperture. We assume that the off-nuclear polarization has the same P.A. of polarization as the AGN polarization. Any value of the P.A. of polarization will produce negligible variations in the estimation of the intrinsic polarization, given the low measured polarization. Using the diffuse stellar emission, $I^{\rm ste}_{K'} = 45 \pm 16$ per cent, relative to the AGN emission, $I^{\rm AGN}_{K'} = 55 \pm 16$ per cent estimated in Section 4.1, we define the ratio of both emission components as $R_{K'} = I^{\rm ste}_{K'}/I^{\rm AGN}_{K'} = 0.8 \pm 0.6$.

As noted in the introduction, previous studies (Young et al. 1995; Packham et al. 1997; Lumsden et al. 1999; Simpson et al. 2002; Watanabe et al. 2003) have shown that the NIR polarization in the nuclear regions of NGC 1068 arises from the passage of light through aligned dust grains in the torus. As we only have polarization measurements in two NIR filters, we cannot estimate the relative contribution of the dichroic absorption to the polarized flux at K'. We therefore resort to previously published results. Young et al. (1995) found that the dichroic absorption mechanism accounts for ∼90 per cent of the polarized flux, with a combination of electron and dust scattering from the ionization cones accounting for ∼10 per cent of the polarized flux at 2.0 μm in a 3.08 arcsec × 3.00 arcsec (185 pc × 180 pc) slit aperture (fig. 6 from Young et al. 1995). Watanabe et al. (2003) found that the dichroic absorption mechanism can account for ∼100 per cent of the polarized flux at 2.2 μm in a 0.88 arcsec × 2.00 arcsec (53 pc × 120 pc) slit aperture (fig. 1 there). These slit sizes are larger than the 0.5 arcsec (30 pc) aperture in our study. The difference in aperture sizes can affect the polarization measurements due to scattered emission from the extended biconical structures around the core of NGC 1068 (Packham et al. 1997; Lumsden et al. 1999; Simpson et al. 2002), and the diffuse stellar emission in the host galaxy. Simpson et al. (2002) showed that the polarized flux from the core of NGC 1068 completely dominates within an aperture <1 arcsec, where contributions from off-nuclear scattered light would be barely detectable. Other polarization components (i.e. electron scattering from the inner regions of the ionization cones and/or dust scattering by large grains in the torus) can contribute, at some level, to the polarized flux at K' within our 0.5 arcsec (30 pc) aperture, however the contribution of these components are highly dependent of the geometry of the system, implying a large amount of assumptions that will introduce high uncertainties in the estimation of the intrinsic polarization. Based on these studies, these polarization mechanisms cannot be ruled out, but the contribution to the polarized flux of these components have not been quantified yet and require more detailed polarization models. We here assume the upper limit of the dichroic absorption to be 100 per cent of the polarized flux, in agreement with the polarization model of Watanabe et al. (2003), i.e. $F^{\rm dic}_{K'} = 1$. The intrinsic polarization at K' arising from dichroic absorption, $P^{\rm int}_{K'}$, is

$$P^{\rm int}_{K'} = (P^{\rm obs}_{K'} - P^{\rm off}_{K'}) \times (1 + R_{K'}) \times F^{\rm dic}_{K'} \quad (1)$$

and is estimated to be $P^{\rm int}_{K'} = 7.0 \pm 2.2$ per cent in a 0.5 arcsec (30 pc) aperture.

5 MAGNETIC FIELD STRENGTH IN THE TORUS

The magnetic field strength in the NIR emitting regions of the torus of NGC 1068 is estimated following similar analysis to that of Lopez-Rodriguez et al. (2013). Specifically, the magnetic field strength is estimated through three different methods: (1) paramagnetic alignment, (2) thermal and magnetic relaxation time equipartition and (3) Chandrasekhar–Fermi method.

5.1 Physical conditions in the torus of NGC 1068

NIR reverberation mapping of several AGNs has shown that the outer radius of the broad-line region (BLR) approximately corresponds to the inner radius of the dusty torus (Suganuma et al. 2006; Koshida et al. 2014). The gas temperature reaches a value of $\sim 10^4$ K in the BLR (Netzer 1987). Krolik & Kriss (2001) suggested that a warm absorber gas in the inner edge of the torus can reach temperatures in the range of 10^4–10^6 K. Based on these previous studies, we adopt the lower limit of the gas temperature to be $T_{\rm gas} = 10^4$ K. We here adopt the CLUMPY torus model[1] by Nenkova et al. (2002, 2008a,b). This model depicts the torus as a distribution of optically thick and dusty clouds surrounding the central engine, instead of homogeneously filling the torus volume. The NIR-emitting region in the torus is identified with clumps directly illuminated by the central engine, with dust grain temperatures below the sublimation temperature in the range of 800–1500 K. The dust grain sizes are assumed to be in the range of 0.005–0.25 μm. Based on the CLUMPY torus description and the further fitting to the nuclear IR spectral energy distribution (SED) of NGC 1068 by Alonso-Herrero et al. (2011) using BAYESCLUMPY (Asensio Ramos & Ramos Almeida 2009), the torus

[1] For details of the CLUMPY torus models see www.clumpy.org

Table 3. Physical parameters of the Torus of NGC 1068.

Description	Parameter	Value
Radial extent of the torus	Y	6^{+2}_{-1}
Width of the angular distribution of clouds	σ	$26^{+6\circ}_{-4}$
Number of clouds along the radial equatorial direction	N_0	14^{+1}_{-3}
Power-law index of the radial density profile	q	$2.2^{+0.4}_{-0.3}$
Inclination of the torus	i	$88^{+2\circ}_{-3}$
Optical depth per single cloud	$\tau_{\rm V}$	49^{+4}_{-3}
Sublimation radius	$r_{\rm sub}$	0.4 pc
Torus height	H	$1.1^{+0.7}_{-0.3}$ pc
Half-opening angle	θ	$64^{+4\circ}_{-6}$
Gas temperature	$T_{\rm gas}$	10^4 K
Grain temperature	$T_{\rm gr}$	800 – 1500 K
Grain size	a	0.005 – 0.25 μm
Number density in the clumps	n	$2.30^{+0.36}_{-0.61} \times 10^5$ cm^{-3}

of NGC 1068 can be described with a radial thickness of $Y = 6^{+2}_{-1}$, angular width of $\sigma = 26^{+6\circ}_{-4}$, number of clouds along the equatorial $N_0 = 14^{+1}_{-3}$, radial density profile with an index of $q = 2.2^{+0.4}_{-0.3}$, viewing angle of $i = 88^{+2\circ}_{-3}$ (almost edge-on), and the optical depth per single cloud of $\tau_{\rm V} = 49^{+4}_{-3}$. The distance of the inner wall of the torus from the black hole, $r_{\rm sub}$, is assumed to be the sublimation distance given by $r_{\rm sub} = 1.3(L_{\rm bol}/10^{46}{\rm ergs}^{-1})^{1/2}(T_{\rm gr}/1500{\rm K})^{-2.8}$ pc (Barvainis 1987). We took the bolometric luminosity of NGC 1068 to be $L_{\rm bol} = 9.55 \times 10^{44}$ erg s^{-1} by Woo & Urry (2002), and we estimated $r_{\rm sub} = 0.4$ pc for dust grains at 1500 K. The torus height is estimated as $H = r_{\rm out} \sin\sigma = 1.1^{+0.7}_{-0.3}$ pc, with $r_{\rm out} = Yr_{\rm sub} = 2$–$3.2$ pc. The half-opening angle of the torus is estimated as $\Theta = 90^\circ - \sigma = 64^{+4\circ}_{-6}$, which is defined with respect to the projected symmetry axis of the CLUMPY model. The number density in the individual clumps of NGC 1068 were calculated assuming the output parameters of the CLUMPY torus models by Alonso-Herrero et al. (2011): (1) a torus radius of $r_{\rm out} = 2.0$–3.2 pc, (2) the number of clouds along the equatorial direction of $N_0 = 14^{+1}_{-3}$ and (3) the optical depth per cloud of $\tau_{\rm v} = 49^{+4}_{-3}$, converted to be $A_{\rm v} = 1.086\tau_{\rm v} = 53^{+4}_{-3}$ mag. Using the standard Galactic ratio $A_{\rm v}/N_{\rm H} = 5.23 \times 10^{-22}$ mag cm^{-22} (Bohlin, Savage & Drake 1978), the column density of the individual clouds is $N_{\rm H} = 1.01^{+0.08}_{-0.06} \times 10^{23}$ cm^{-2}. The number density in the individual clouds in the torus are estimated to be $n = N_{\rm H}/(r_{\rm out}/N_0) = 2.30^{+0.36}_{-0.61} \times 10^5$ cm^{-3}, which compare very well with the number density in the range of 10^4–10^5 cm^{-3} for molecular clouds in Orion A, M17 and Cepheus A (e.g. Goldsmith 1999). A summary of the physical parameters of the torus is shown in Table 3.

5.2 Method 1: paramagnetic alignment

We concluded that the NIR polarization arises from the passage of radiation through aligned dust grains in the clumps of the torus of NGC 1068 (Section 4.2). Non-spherical spinning dust grains can become aligned in the presence of a magnetic field, a process termed paramagnetic alignment (Davis & Greenstein 1951). If the dust grains are aligned by this mechanism, then some degree of polarization through dichroic absorption and/or emission can be measured. This measurement can be used to estimate the strength and geometry of the magnetic field. In case of the geometry, the long axes of the dust grains are aligned perpendicular to the direction of the magnetic field. A P.A. of polarization parallel to the magnetic field is expected for dichroic absorption. In case of the magnetic field strength, if paramagnetic alignment is the dominant mechanism, then the dust grain alignment efficiency is given by the ratio of the degree of polarization, P(per cent), and the extinction, $A_{\rm V}$, and is related to the magnetic field strength, B, as shown by Jones & Spitzer (1967), and adapted by Vrba, Coyne & Tapia (1981) and Lopez-Rodriguez et al. (2013):

$$P({\rm per\ cent})/A_{\rm V} = \frac{67\chi'' B^2}{75a\omega n}\left(\frac{2\pi}{m_{\rm H}kT_{\rm gas}}\right)^{1/2}(\gamma - 1) \times \left(1 - \frac{T_{\rm gr}}{T_{\rm gas}}\right) \quad (2)$$

χ'' is the imaginary part of the complex electric susceptibility, a measure of the attenuation of the wave caused by both absorption and scattering, B is the magnetic field strength, γ is the ratio of inertia momentum around the two major axes of the dust grains, $T_{\rm gr}$ is the dust grain temperature, a is the dust grain size, ω is the orbital frequency of the dust grains, n is the number density in the cloud, $m_{\rm H}$ is the mass of a hydrogen atom, k is the Boltzmann constant and $T_{\rm gas}$ is the gas temperature.

Davis & Greenstein (1951) showed that the lower bound of the ratio χ''/ω for most interstellar grains is

$$\frac{\chi''}{\omega} = 2.5 \times 10^{-12}\ T_{\rm gr}^{-1}. \quad (3)$$

The ratio of the moments of inertia of the dust grains, γ, is defined as

$$\gamma = \frac{1}{2}\left[\left(\frac{b}{a}\right)^2 + 1\right], \quad (4)$$

where b/a is the dust grain axial ratio. A typical value of b/a for interstellar dust grains is ∼0.2 (Aannestad & Purcell 1973; Kim & Martin 1995). It should be noted that the real dust composition in AGN might be more complex than the typical interstellar dust grains, as several authors suggest (e.g. Maiolino et al. 2001a; Maiolino, Marconi & Oliva 2001b; Hatziminaoglou E. et al. 2015).

The magnetic field strength is estimated using the physical conditions in Table 3, the intrinsic polarization at K' arising from dichroic absorption of $P^{\rm int}_{K'} = 7.0 \pm 2.2$ per cent (Section 4.2), and the extinction to the central engine $A_{\rm V} = 36$ mag (Packham et al. 1997)

converted[2] to $A_{K'} = 4.03$ mag. The extinction represents the closest measurement at our observations, and it has been previously used by Watanabe et al. (2003). Imanishi et al. (1997) estimated a visual extinction in the range of 17–30 mag using the 3.4 μm absorption feature of the NIR (2.9–4.1 μm) spectroscopic observations on the 1.5-m telescope on Mount Lemmon, Arizona, USA. These measured visual extinctions are lower than the whole visual extinction of the clouds, $A_{\rm v} = 53^{+4}_{-3}$ mag. (Section 5.1), estimated using the CLUMPY model to the IR SED of NGC 1068, indicating that we are possibly seeing the radiation from the clouds and/or central engine passing through a section of the clouds (Section 6.1). Based on the range of the physical parameters shown in Table 3, the magnetic field strength is estimated to be in the range of 4–82 mG for the NIR emitting regions in the torus of NGC 1068. The magnetic field strength in the maser emission of NGC 1068 was estimated to be 71 and 3 mG for standard accretion disc and advection-dominated accretion flow model, respectively (Gnedin et al. 2014). Several studies (e.g. Herrnstein et al. 1998; Kartje et al. 1999; Modjaz et al. 2005) have shown that the magnetic field strength is in the range of 2–300 mG at scales of 0.1–1 pc from the central engine of AGN. Although these measurements were done for different objects, our estimated magnetic field strength in the torus of NGC 1068 is in agreement with the typical magnetic field strengths in the surrounding areas of the accretion disc in AGNs.

Several assumptions were made in the estimation of the magnetic field strength in the torus of NGC 1068. Here, we consider each of these assumptions in detail. The physical conditions in molecular clouds make the alignment of dust grains less responsive to the magnetic field (i.e. Gerakines, Whittet & Lazarian 1995; Lazarian 1995). However, the dust grains in the dusty torus of AGN certainly experience much more turbulence and extreme physical conditions than in molecular clouds, and the dust alignment is more sensitive to the magnetic field strength (Section 5.3, 6.1).

We assumed a homogeneous magnetic field, where any inhomogeneities of the magnetic field in the torus are ignored. This assumption has some implications for the ratio P(per cent)/$A_{\rm V}$. If a homogeneous magnetic field is responsible for dust grains' alignment in the torus, then all the dust grains will be aligned along the same direction of the magnetic field. In this case, the alignment efficiency, P(per cent)/$A_{\rm V}$, is maximal. The degree of polarization would decrease when inhomogeneities of the magnetic field are present (Section 6.1). This method shows a strong dependence on dust grain sizes. The grain size distribution in the clumps is poorly constrained, which makes it difficult to quantify the uncertainties introduced in the estimations of the magnetic field strength.

5.3 Method 2: thermal and magnetic relaxation time equipartition

The approach followed in Method 1 (Section 5.2) is valid only when the ratio of thermal to magnetic pressure is smaller than unity (Gerakines et al. 1995), meaning that the magnetic field is dominant. Under this condition, the magnetic field is strong enough to align the dust grains faster than the rotational kinetic energy. The magnetic relaxation time is required to be shorter than the thermal relaxation time, i.e. $t_{\rm m} < t_{\rm th}$. To verify this condition, we calculate the required lower limit magnetic field strength given by (section 7.2 from Lopez-Rodriguez et al. 2013)

$$B^2 > 2.4 \times 10^{11} a n m_{\rm H} T_{\rm gr} \left(\frac{8kT_{\rm gas}}{\pi m_{\rm H}} \right)^{1/2}. \quad (5)$$

The magnetic field strength is estimated to be >6 mG for the physical conditions shown in Table 3. Under the condition that the magnetic relaxation time is shorter than the thermal relaxation time, the gas and dust are decoupled. This result has two implications: (1) it is only valid in low-density regions of the clouds, and (2) the ratio P(per cent)/$A_{\rm v}$ is dependent on the magnetic field strength. Thus, we conclude that the detected NIR polarization arises from the passage of NIR radiation through the low-density regions of the clumps in the torus. Otherwise, the NIR radiation would be completely extinguished (Section 6.1). This scheme satisfies condition (1) and the estimation of the magnetic field strength in method 1 (Section 5.2) is allowed.

5.4 Method 3: Chandrasekhar–Fermi method

The Chandrasekhar–Fermi method (Chandrasekhar & Fermi 1953, hereafter CF method) gives us an alternative estimation of the magnetic field strength. Specifically, the CF method relates the magnetic field strength with the dispersion in polarization angles, α, of the constant component of the magnetic field, and the velocity dispersion of the gas. We use the adapted version of Ostriker, Stone & Gammie (2001), where they introduced the factor of 0.5 in the CF method to compensate for averaging along the LOS.

$$B = 0.5 \left(\frac{4}{3} \pi \rho \right)^{1/2} \frac{\sigma_{\rm v}}{\alpha} \ [\mu{\rm G}], \quad (6)$$

where ρ is the volume mass density in g cm^{-3}, $\sigma_{\rm v}$ is the velocity dispersion in cm s^{-1} and α is the dispersion of polarization angles in radians. The volume mass density was calculated using the number density in Table 3 multiplied by the weight of molecular hydrogen. Greenhill et al. (1996) estimated velocity dispersions up to 100 km s^{-1} of the Very Large Baseline Interferometry (VLBI) H_2O masers at scales of 0.65 pc from the central engine of NGC 1068 using VLBI. We note that these results are higher than the typical velocity dispersion of 10 km s^{-1} used in previous MHD outflow wind models (e.g. Elitzur & Shlosman 2006), which can yield higher estimations of the magnetic field strength.

As the AGN in NGC 1068 is unresolved, the polarization vectors are average values of the LOS to the nucleus. If we average the LOS across the observed core (Fig. 2), it will provide an insignificant dispersion in P.A. This measurement will yield unrealistically large magnetic field strengths with the CF method. Hence, the dispersion of P.A., α, cannot be measured directly from the observed dispersion of the polarization vectors across the core of NGC 1068 at K'. We need another approach to estimate α; we used the model by Jones et al. (1992, hereafter JKD). This model relates the degree of polarization at K with the level of turbulence in the interstellar medium and the magnetic field. The magnetic field is assumed to have a constant and a random component. For NGC 1068, using the intrinsic polarization arising from dichroic absorption at K', $P^{\rm int}_{K'} = 7.0 \pm 2.2$ per cent (Section 4.2), and the extinction to the central engine, $A_{\rm v} = 36$ mag (Packham et al. 1997), converted[3] to be $\tau_K = 3.24$, we found that our data in the JKD model is close to

[2] The conversion of visual extinction, $A_{\rm V}$, to extinction at K, A_K, is $A_K = 0.112 A_{\rm V}$ (Jones 1989).

[3] The conversion of visual extinction, A_K, to optical depth at K, $\tau_K = 0.09 A_{\rm v}$ (Jones 1989).

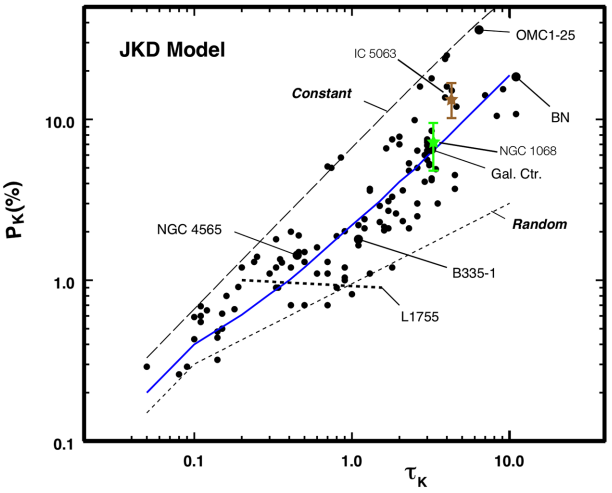

Figure 3. Degree of polarization at K versus optical depth. Plotted is the data compilation from Jones (1989, black dots) with some specific objects labelled. The upper (long dash) line is the JKD model result assuming only a constant component to the magnetic field ($P = \tanh(\tau_P)$). The bottom (short dash) line corresponds to a purely random magnetic field with a decorrelation length of $\tau_K = 0.1$ ($P \propto \tau^{1/2}$). The solid blue line results from a 50/50 mix of constant and random components and fits the overall trend in the data well. The data point for IC 5063 is plotted as a brown star (Lopez-Rodriguez et al. 2013). The estimated intrinsic polarization for NGC 1068 from this work, $P^{\rm int}_{K'} = 7.0 \pm 2.2$ per cent (Section 4.2) with $A_V = 36$ from (Packham et al. 1997), is plotted as a green star.

equal contribution of the constant and random components of the magnetic field (Fig. 3). For our data point in Fig. 3, if we assume that the constant component of the magnetic field is in the plane of the sky, the dispersion of polarization angles is estimated to be $\alpha = 7^\circ\!.0$ (0.1221 radians) using fig. 9 by JKD. We substituted the above numerical values in equation (6), and estimated a lower limit of the magnetic field strength in the plane of the sky in the range of 52^{+4}_{-8} mG, depending on the conditions in the torus.

We assumed that the constant component of the magnetic field strength is in the plane of the sky. If the constant component of the magnetic field is away from the plane of the sky, then the magnetic field strength will be underestimated. For example, if the magnetic field is pointing along our LOS, zero polarization will be measured. Since NGC1068 is classified as a type 2 AGN, the torus axis is in the plane of the sky. This geometry favours the assumption of the constant component of the magnetic field to be in the plane of the sky. We note that the all-sky *Planck* polarization data (Planck Collaboration XIX 2014) shows some objects with polarization measurements above the theoretical polarization maximum in the JKD model. However, it is difficult to compare the *Planck* results with ours, given that *Planck*'s beam of 5 arcmin does not resolve AGNs.

A summary of the estimations of the magnetic field strengths through the different methods presented in Section 5 is shown in Table 4. The modified CF method described in Section 6.1 is also included.

Table 4. Estimations of the magnetic field strength.

Method	B (mG)
1: Paramagnetic alignment	4–82
2: Thermal and magnetic equipartition	>6
3: Chandrasekhar–Fermi method	52^{+4}_{-8}
4: Modified Chandrasekhar–Fermi method[a]	139^{+11}_{-20}

Notes. [a]Modified CF Method is calculated as $B' = B \times \beta^{-1/2}$, with $\beta = 0.15$ (Section 6.1).

6 DISCUSSION

6.1 Magnetic field in the torus of NGC 1068

As discussed in Section 4.2, the measured polarization arises from the passage of radiation through aligned dust grains in the torus of NGC 1068. As the grain alignment occurs with the long axes perpendicular to the magnetic field, a measured P.A. of polarization parallel to the magnetic field is expected for dichroic absorption. We interpret the measured P.A. of polarization at K' in a 0.5 arcsec (30 pc) aperture, P.A.$_{K'} = 127^\circ \pm 2^\circ$, as the orientation of the magnetic field in the torus of NGC 1068. We took the orientation of the torus to be PA$_{\rm torus} \sim -42^\circ$ (measured anticlockwise, for direct comparison with our P.A.$_{K'}$, then PA$_{\rm torus} \sim -42^\circ + 180^\circ = 138^\circ$) from Raban et al. (2009), and we found that the PA$_{\rm torus} \sim$ P.A.$_{K'}$. The constant component of the magnetic field is thus aligned with the torus axis. Our result implies that our measured P.A. of polarization gives us direct information on the existence and geometry of the torus. Specifically, the polarization signature of the parsec-scale structure, identified as the obscuring torus, is observed through NIR polarization and direct spatial comparison between IR interferometric and IR polarimetric observations can be made. Based on these results, the misalignment of ∼49° between the measured P.A. of polarization and the radio jet axis (Section 3, Fig. 2) can be interpreted as the misalignment between the torus (assuming that the torus axis is in the plane of the sky) and the radio jet axis. Thus, physical components far below the spatial resolution of the NIR polarimetric observations can be estimated.

As noted in Section 5.4, we assumed the magnetic field as a mix of a turbulent and a constant component, where the turbulent component can be in any orientation. To infer the relative contribution of both components, we used the method presented by Hildebrand et al. (2009). These authors showed that the ratio of turbulent to constant components of the magnetic field strength, $\langle B_{\rm t}^2\rangle^{1/2}/B_o$, is a function of the dispersion of the plane of polarization, α, given by

$$\frac{\langle B_{\rm t}^2\rangle^{1/2}}{B_o} = \frac{\alpha}{\sqrt{2-\alpha^2}}. \quad (7)$$

Using the dispersion of the plane of polarization $\alpha = 7^\circ$ (0.1221 radians) from Section 5.4, the ratio of turbulent to constant components of the magnetic field strength is $\langle B_{\rm t}^2\rangle^{1/2}/B_0 = 0.09$. Thus, the constant component, with a toroidal geometry, is dominant in the torus of NGC 1068.

The misalignments of the structures in the inner few parsecs of NGC 1068 can produce local inhomogeneities in the magnetic field. These inhomogeneities produce an underestimation of the magnetic field strength measured through the paramagnetic alignment (Section 5.2). This underestimation of the magnetic field strength can explain the similarity of the paramagnetic alignment and the thermal and magnetic relaxation time equipartition. Thus, a higher magnetic field strength should be expected. The CF method assumed thermal and magnetic pressure equipartition. Kudoh & Basu (2003) showed that the equipartition is not satisfied in all regions of the molecular

clouds and the CF method must be refined/modified in such regions. They defined the thermal to magnetic pressure ratio, β, as

$$\beta = \frac{c_s^2}{V_A^2} = \frac{\rho c_s^2}{(B^2/4\pi)}, \quad (8)$$

where c_s is the sound speed defined as $c_s = \sqrt{kT/m}$, k is the Boltzmann constant, T is the gas temperature and m is the mean molecular mass. V_A is the Alfvén speed, defined as $V_A = B/\sqrt{4\pi\rho}$, ρ is the cloud density and B is the magnetic field strength.

The dimensionless β parameter is typically used in MHD simulations (i.e. Ostriker et al. 2001; Kudoh & Basu 2003) to account for the magnetization of the molecular clouds. Three different situations can be found: (1) $\beta \gg 1$ is considered as low magnetization, (2) $\beta \sim 1$ represents the equipartition between dynamic and magnetic pressure (CF method condition) and (3) $\beta \sim 0$ is considered as high magnetization. Kudoh & Basu (2003) found that the dynamic and magnetic pressure ratio is in approximate equipartition, $\beta \sim 1$, in the regions containing most of the mass of the molecular clouds. However, $\beta < 1$ in the low-density outer regions of the clouds.

Using the magnetic field strength, $B = 52^{+4}_{-8}$ mG from the CF method, and the cloud density from Section 5.4, we find $\beta \sim 0.15$. This value suggest that the clumps in the torus of NGC 1068 are in a highly magnetic environment. Another implication of $\beta \sim 0.15$ is that the polarization is arising from the low-density regions of the clumps. This physical condition agrees with the conditions of the paramagnetic alignment mechanism (Section 5.3). Thus, the magnetic field strength estimated through the CF method should be refined using the β parameter. The modified CF method is given by $B' = B \times \beta^{-1/2}$ (Ostriker et al. 2001), which yields a magnetic field strength $B' = 139^{+11}_{-20}$ mG (Table 4).

We interpret these results as: (1) the NIR total flux comes from the directly illuminated clumps located above the equatorial plane affording a direct view into our LOS, i.e. the surface of the clumps that are directly illuminated by the central engine (e.g. Hönig et al. 2008; Heymann & Siebenmorgen 2012; Stalevski et al. 2012), (2) the NIR radiation passes through the low-density outer layers of the clumps and (3) NIR polarization arises from the passage of radiation through the aligned dust grains in the clumps. These dust grains are aligned by a global toroidal magnetic field in the torus generated by the accretion disc. The clumps located above the equatorial plane, those clumps in equation (1), have higher likelihood of escaping photons along our LOS than those located close to the equatorial plane. A sketch is shown in Fig. 4.

6.2 Hydromagnetic wind

Within the MHD framework (e.g. Blandford & Payne 1982; Emmering et al. 1992; Contopoulos 1994; Kartje et al. 1999), the magnetic field plays an important role in the dynamics of the clumps in the torus. The inflow/outflow mass rates for those clumps showing NIR dichroic absorption are estimated assuming a hydromagnetic wind model. The mass accretion rate as a function of the magnetic field strength can be estimated through the thermal and magnetic pressure ratio. The thermal pressure on the mid-plane (Frank, King & Raine 1992) is given by

$$P_{th} = \rho c_s^2 = \frac{G M_{BH} \dot{M}}{3\pi\sqrt{2\pi} c_s r^3 \alpha_s}, \quad (9)$$

where M_{BH} is the black hole mass, $\dot{M}$ is the mass accretion rate in units of $M_\odot\ yr^{-1}$, r is the distance from the black hole in units of parsecs, and α_s is the Shakura–Sunyaev (Shakura & Sunyaev 1973) viscosity parameter.

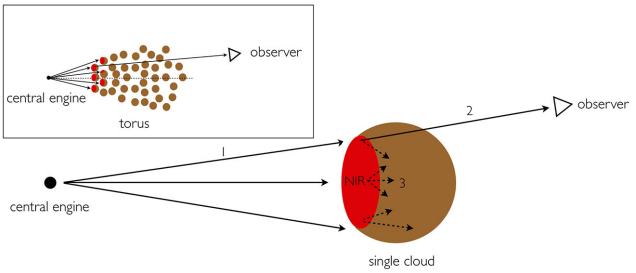

Figure 4. Sketch of a single cloud and its location within the torus (box). (1) The NIR total flux comes from the directly illuminated clumps located above the equational plane affording a direct view into our LOS, i.e. the surface of the clumps that are directly illuminated by the central engine (Hönig et al. 2008), (2) the NIR radiation passes through the low-density outer layers of the clumps, and (3) NIR polarization arises from the passage of radiation through the aligned dust grains in the clumps (Section 6.1).

As described in Section 6.1, the thermal and magnetic pressure equipartition was defined as $\beta = P_{th}/P_B$, which can be used in equation (9) to estimate the mass accretion rate as a function of the magnetic field:

$$\dot{M} = \frac{3\sqrt{2\pi} c_s r^3 B^2 \alpha_s \beta}{8 G M_{BH}}. \quad (10)$$

The parameters α_s and β are related through the MHD simulations prescription $\alpha_s = C/(1+\beta)$, where C is a constant typically set in the range of 0.5–0.6 (Narayan et al. 1998). This relation is satisfied if magnetic fields provide the kinematic viscosity, which is the case in the magnetic environment in the clumps, $\beta \sim 0.15$, estimated in Section 6.1. In this context, the viscosity parameter is estimated to be $\alpha_s = 0.48 \pm 0.05$. We use the magnetic field strength estimated to be in the range of $B = 4$–139 mG (Section 6). We took the black hole mass of NGC 1068 $M_{BH} = (8.0 \pm 0.3) \times 10^6\ M_\odot$ from Lodato & Bertin (2003). These authors fitted a self-gravitating accretion disc model to the observed non-Keplerian rotational curve of the maser disc to derive the black hole mass in NGC 1068. From the physical interpretation presented in Section 6.1, the NIR emitting region arises from the directly illuminated faces of the clumps located as $r_{sub} = 0.4$ pc for dust grains at 1500 K (Section 5.1).

The clumps with measured NIR dichroism were assumed to be above the equatorial plane (Fig. 4), these clumps are located in the inner edge of the torus, with a vertical height of $H = r_{sub} \sin\sigma = 0.17^{+0.04}_{-0.02}$ pc. As a first approximation, the balance of magnetic and thermal pressure on the mid-plane allow us to estimate upper limits of the mass accretion/outflow rates. Based on these conditions and using equation (10), we estimate the upper limit of the mass accretion rate to be

$$\dot{M} \leq 8 \times 10^{-3} \left(\frac{r}{0.4\ \mathrm{pc}}\right)^3 \left(\frac{T}{1500\ \mathrm{K}}\right)^{1/2} \left(\frac{B}{139\ \mathrm{mG}}\right)^2 \times \left(\frac{M_{BH}}{8.0 \times 10^6\ M_\odot}\right)^{-1} M_\odot\ yr^{-1}. \quad (11)$$

For the canonical values in equation (11), the mass accretion rate is $\dot{M} \leq 8 \times 10^{-3}\ M_\odot\ yr^{-1}$ at a distance of 0.4 pc from the central engine of NGC 1068. As we only have physical information of those clouds within the outflow where we measure NIR dichroism, the estimated inflow/outflow mass accretion rate represents only a

fraction of the black hole mass accretion rate, $\dot{M} = 0.18$ $M_\odot\ yr^{-1}$, calculated using the bolometric luminosity, $L_{bol} = 9.55 \times 10^{44}$ erg s^{-1} (Woo & Urry 2002), of NGC1068.

Elitzur & Shlosman (2006) showed that the mass outflow wind rate, $\dot{M}_w$, and mass accretion rate, $\dot{M}$, can be related as

$$\dot{M}_w \leq 0.14 \left(\frac{T}{1500\ K}\right)^{-2.6} \left(\frac{N_H}{10^{23}\ cm^{-2}}\right) \times \left(\frac{v}{100\ km\ s^{-1}}\right) I_1 (\epsilon \dot{M})^{1/2}\ M_\odot\ yr^{-1}, \quad (12)$$

where N_H is the total column density normalized to 10^{23} cm^{-2}, v is the velocity at the inner radius of the torus normalized to 100 km s^{-1} based on H_2O maser VLBI observations of NGC 1068 at ∼0.4 pc by Greenhill et al. (1996), ϵ is the accretion efficiency at the torus radii and I_1 is an unknown factor of order unity (section 6.1 in Nenkova et al. 2008b).

We took the total column density, $N_H = 1.41^{+0.22}_{-0.37} \times 10^{24}$ cm^{-2} (Section 5.1), the velocity of 100 km s^{-1}, the accretion efficiency at the torus inner radius of $\epsilon = 0.01$, typically used at the torus scales by Emmering et al. (1992) and Elitzur & Shlosman (2006), and we obtain an upper-limit of the mass outflow rate of $\dot{M}_w \leq$ 0.17 $M_\odot\ yr^{-1}$ at a distance of 0.4 pc from the central engine of NGC 1068.

The torus outflow time-scale is $t_w = M_{torus}/\dot{M}_w$. M_{torus} is the torus mass given by $M_{torus} = m_p N_H \int N_{cl} dV \sim 10^3 N_{H,\,23} L_{45} Y\ M_\odot$ (Elitzur & Shlosman 2006), where L_{45} is the bolometric luminosity normalized to 10^{45} erg s^{-1}, and Y is the torus radial thickness. We took the bolometric luminosity to be $L_{bol} = 9.55 \times 10^{44}$ erg s^{-1} (Woo & Urry 2002), and $Y = 6^{+2}_{-1}$ (Section 5.1), and we estimate the mass of the torus to be $M_{torus} = 6.73^{+1.08}_{-1.74} \times 10^4\ M_\odot$. This value is within a factor of 3 lower than $M_{torus} = 2.4 \times 10^5\ M_\odot$ using radio observations by Gallimore et al. (1996) and $M_{torus} = 2.1(\pm 1.2) \times 10^5\ M_\odot$ using mm-observations with ALMA by García-Burillo et al. (2014). The difference in torus mass can be interpreted as the CLUMPY torus fitting to the IR (1–20 μm) SED is only accounting for those clouds emitting in the IR, where a more compact torus would be detected. The outflow time-scale is estimated to be $t_w \geq 10^5$ yr. If we assume a torus rotating around the accretion disc with a typical Keplerian orbit of $t_K = 3 \times 10^4 M_{BH,7}^{-1/2} r_{pc}^{3/2}$ yr (Elitzur & Shlosman 2006), the time-scale to complete a Keplerian orbit at 0.4 pc from the central engine is $t_K \sim 10^3$ yr. Thus, the obscuring structure of NGC 1068, generated by the outflowing wind, can be created in ≥100 Keplerian orbits, yielding a rotational velocity ≤1228 km s^{-1}. These results suggest that the outflowing wind, generated by the accretion disc's magnetic field, can rapidly create an dusty obscuring structure around the central engine of NGC 1068. Recent time-resolving 3D hydrodynamical models of AGN (Schartmann et al. 2014) found that the radiation of the central engine powers a loss of mass with a rate of 0.1 $M_\odot\ yr^{-1}$, with similar inflow mass rates from large scales in order to keep the dusty structure lifetime for a period of ∼10 Myr. In addition, some models assuming gas accretion flows, such as adiabatic inflow–outflow solutions (Blandford & Begelman 1999) and convection-dominated accretion flows (Narayan, Igumenshchev & Abramowicz 2000), suggest that only a small fraction of the accreted matter at the outer radius of the inflow contributes to the mass accretion rate at the black hole. This can be explained by turbulence and strong mass lost. In this scheme, the accreting efficiency is low ($\epsilon \sim 0.01$) at the outer radius of the inflow, favouring the outflow wind. This scenario should be examined in a sample of AGNs to find general and/or extraordinary properties of the outflowing wind model.

7 CONCLUSIONS

We found that the existence and evolution of the torus in NGC 1068 can be explained through the hydromagnetic outflowing model of AGNs. Assuming CLUMPY torus models, the polarization of NGC 1068 in the K' filter is most likely arising from radiation of the directly illuminated inner-facing clumps of the torus passing through the magnetically aligned dust grains located in the low-density outer regions of the clumps. We found that the constant component of the magnetic field in the plane of the sky is dominant and responsible for the dust grain alignment in the torus with a strength in the range of 4–139 mG. We presented a direct comparison between the P.A. of the NIR polarimetric and IR interferometric observations of NGC 1068. Specifically, a toroidal geometry is the most likely configuration of the magnetic field in the torus. Adopting the estimated magnetic field configuration, we find a mass outflow rate of ≤0.17 $M_\odot\ yr^{-1}$ at a distance of 0.4 pc from the central engine. At this rate, the obscuring structure around the central engine can be created in a time-scale of ≥10^5 yr with a rotational velocity of ≤1228 km s^{-1}. We conclude that the origin, evolution and kinematics of the dusty environment obscuring the central engine of NGC 1068 can be explained by a hydromagnetic outflow wind. Further NIR polarimetric observations of a sample of AGNs are required to refine and/or modify this approach and find general and/or extraordinary magnetic properties in the torus. In addition, MIR polarimetric observations are essential to test the effects of dichroism at longer wavelengths. Also, mm-polarimetric observations with ALMA will allow us to refine intrinsic properties of the torus, i.e. dust density, grain sizes, temperature, used to estimate the magnetic field strength through the different approaches presented in this work, as well as, to test the MHD outflow wind model for those clumps at the outer edge of the torus.

ACKNOWLEDGEMENTS

The authors would like to thank the anonymous referee for the helpful comments. It is a pleasure to acknowledge discussion with R. Antonucci, T. Díaz-Santos, M. Imanishi, M. Kishimoto and M. Stalevski. This work is based on observations made with the 6.5-m MMT, Arizona, USA. ELR and CP acknowledge support from the University of Texas at San Antonio. CP acknowledges support from NSF-0904421 grant. CP and TJJ acknowledge support from NSF-0704095 grant. AA-H acknowledges financial support from the Spanish Plan Nacional de Astronomía y Astrofisíca under grant AYA2012-31447. NAL and REM are supported by the Gemini Observatory, which is operated by the Association of Universities for Research in Astronomy, Inc., on behalf of the international Gemini partnership of Argentina, Australia, Brazil, Canada, Chile, and the United States of America. RN acknowledges support by FONDECYT grant No. 3140436. CRA is supported by a Marie Curie Intra European Fellowship within the 7th European Community Framework Programme (PIEF-GA-2012-327934).

REFERENCES

Aannestad P. A., Purcell E. M., 1973, ARA&A, 11, 309
Alonso-Herrero A. et al., 2011, ApJ, 736, 82
Antonucci R., 1993, ARA&A, 31, 473
Antonucci R. R. J., Miller J. S., 1985, ApJ, 297, 621
Antonucci R., Hurt T., Miller J., 1994, ApJ, 430, 210
Asensio Ramos A., Ramos Almeida C., 2009, ApJ, 696, 2075

Barvainis R., 1987, ApJ, 320, 537
Blandford R. D., Begelman M. C., 1999, MNRAS, 303, L1
Blandford R. D., Payne D. G., 1982, MNRAS, 199, 883
Bohlin R. C., Savage B. D., Drake J. F., 1978, ApJ, 224, 132
Brindle C., Hough J. H., Bailey J. A., Axon D. J., Ward M. J., Sparks W. B., McLean I. S., 1990, MNRAS, 244, 577
Burtscher L. et al., 2013, A&A, 558, 149
Capetti A., Axon D. J., Macchetto F., Sparks W. B., Boksenberg A., 1995, ApJ, 446, 155
Chandrasekhar S., Fermi E., 1953, ApJ, 118, 113
Contopoulos J., 1994, ApJ, 432, 508
Davis L., Jr, Greenstein J. L., 1951, ApJ, 114, 206
Efstathiou A., MacCall A., Hough J. H., 1997, MNRAS, 285, 102
Elitzur M., Shlosman I., 2006, ApJ, 648, L101
Emmering R. T., Blandford R. D., Shlosman I., 1992, ApJ, 385, 460
Evans I. N., Ford H. C., Kinney A. L., Antonucci R. R. J., Armus L., Caganoff S., 1991, ApJ, 369, L27
Frank J., King A., Raine D., 1992, Accretion Power in Astrophysics, 2nd edn. Cambridge Univ. Press, Cambridge
Gallimore J. F., Baum S. A., O'Dea C. P., Pedlar A., 1996, ApJ, 458, 136
García-Burillo S. et al., 2014, A&A, 567, 125
Gerakines P. A., Whittet D. C. B., Lazarian A., 1995, ApJ, 455, 171
Gnedin Yu N., Globina V. N., Piotrovich M. Yu., Buliga S. D., Natsvlishvili T. M., 2014, Astrophysics, 57, 163
Goldsmith P. F., 1999, in Wall W. F., Carramiana A., Carrasco L., eds, Astrophysics and Space Science Library, Vol. 241, Millimeter-Wave Astronomy: Molecular Chemistry & Physics in Space. Kluwer, Dordrecht, p. 57
Gratadour D., Rouan D., Mugnier L. M., Fusco T., Clénet Y., Gendron E., Lacombe F., 2006, A&A, 446, 813
Greenhill L. J., Gwinn C. R., Antonucci R., Barvainis R., 1996, ApJ, 472, L21
Hatziminaoglou E., Hernán-Caballero A., Feltre A., Piñol Ferreo N., 2015, ApJ, 803, 110
Herrnstein J. R., Moran J. M., Greenhill L. J., Blackman E. G., Diamond P., 1998, ApJ, 508, 243
Heymann F., Siebenmorgen R., 2012, ApJ, 751, 27
Hildebrand R. H., Kirby L., Dotson J. L., Houde M., Vaillancourt J. E., 2009, ApJ, 696, 567
Hönig S., Prieto M. A., Beckert T., 2008, A&A, 485, 2008
Ichikawa K. et al., 2015, ApJ, 803, 57
Imanishi M., Terada H., Sugiyama K., Motohara K., Goto M., Maihara T., 1997, PASJ, 49, 69
Jaffe W. et al., 2004, Nature, 429, 47
Jones T. J., 1989, ApJ, 346, 728
Jones R. V., Spitzer L., Jr, 1967, ApJ, 147, 943
Jones T. J., Klebe D., Dickey J. M., 1992, ApJ, 389, 602 (JKD)
Kartje J. F., Konigl A., Elitzur M., 1999, ApJ, 513, 180
Kim J., Martin P. G., 1995, ApJ, 444, 293
Konigl A., Kartje J. F., 1994, ApJ, 434, 446
Koshida S. et al., 2014, ApJ, 788, 159
Krolik J. H., Begelman M., 1988, ApJ, 329, 701
Krolik J. H., Kriss G. A., 2001, ApJ, 561, 684
Kudoh T., Basu S., 2003, ApJ, 595, 892
Lawrence A., 1991, MNRAS, 252, 586
Lazarian A., 1995, 453, 229
Lebofsky M. J., Kemp J. C., Rieke G. H., 1978, ApJ, 222, 95
Lodato G., Bertin G., 2003, A&A, 398, 517
Lopez-Rodriguez E. et al., 2013, MNRAS, 431, 2723
Lumsden S. L., Moore T. J. T., Smith C., Fujiyoshi T., Bland-Hawthorn J., Ward M. J., 1999, MNRAS, 303, 209
Maiolino R., Marconi A., Salvati M., Risaliti G., Severgnini P., Oliva E., La Franca F., Vanzi L., 2001a, A&A, 365, 28
Maiolino R., Marconi A., Oliva E., 2001b, A&A, 365, 37
Markowitz A. G., Krumpe M., Nikutta R., 2014, MNRAS, 439, 1403
Mason R. E., Geballe T. R., Packham C., Levenson N. A., Elitzur M., Fisher R. S., Perlman E., 2006, ApJ, 640, 612
Miller J. S., Antonucci R. R. J., 1983, ApJ, 271, 7
Modjaz M., Moran J. M., Kondratko P. T., Greenhill L. J., 2005, ApJ, 626, 104
Narayan R., Mahadevan R., Grindlay E., Popham R. G., Gammie C., 1998, ApJ, 492, 554
Narayan R., Igumenshchev I. V., Abramowicz M. A., 2000, ApJ, 539, 798
Nenkova M., Ivezic Z., Elitzur M., 2002, ApJ, 570, L9
Nenkova M., Sirocky M. M., Ivezic Z., Elitzur M., 2008a, ApJ, 685, 145
Nenkova M., Sirocky M. M., Nikutta R., Ivezic Z., Elitzur M., 2008b, ApJ, 685, 160
Netzer H., 1987, MNRAS, 225, 55
Ostriker E. C., Stone J. M., Gammie C. F., 2001, ApJ, 546, 980
Packham C., Jones T. J., 2008, Proc. SPIE, 7014, 82
Packham C., Hough J. H., Young S., Chrysostomou A., Bailey J. A., Axon D. J., Ward M. J., 1996, MNRAS, 278, 406
Packham C., Young S., Hough J. H., Axon D. J., Bailey J. A., 1997, MNRAS, 288, 375
Packham C., Radmoski J. T., Roche P. F., Aitken D. K., Perlman E., Alonso-Herrero A., Colina L., Telesco C. M., 2005, MNRAS, 618, 17
Packham C., Jones T. J., Krejny M., DeWahl K., Warner C., Lopez Rodriguez E., 2012a, Proc. SPIE, 7735, 6
Packham C., Jones T. J., Warner C., Krejny M., Shenoy D., Vonderharr T., Lopez-Rodriguez E., DeWahl K., 2012b, Proc. SPIE, 8446, 3
Planck Collaboration XIX, 2014, A&A, 576, A104
Raban D., Jaffe W., Röttgering H., Meisenheimer K., Tristram K. R. W., 2009, MNRAS, 394, 1325
Radomski J. T., Pina R. K., Packham C., Telesco C. M., Tadhunter C. N., 2002, ApJ, 566, 675
Radomski J. T., Pina R. K., Packham C., Telesco C. M., De Buizer J. M., Fisher R. S., Robinson A., 2003, ApJ, 587, 117
Radomski J. T. et al., 2008, ApJ, 681, 141
Ramos Almeida C. et al., 2009, ApJ, 702, 1127
Ramos Almeida C. et al., 2011, ApJ, 731, 92
Rouan D., Rigaut F., Alloin C., Doyon R., Lai O., Crampton D., Gendron E., Arsenault R., 1998, A&A, 339, 687
Rouan D. et al., 2004, A&A, 414, L1
Schartmann M., Krause M., Burkert, 2011, MNRAS, 415, 741
Schartmann M., Wada K., Prieto M. A., Burkert A., Tristram K. R. W., 2014, MNRAS, 445, 3878
Shakura N. I., Sunyaev R. A., 1973, A&A, 24, 337
Simpson J. P., Colgan S. W. J., Erickson E. G., Hines D. C., Schultz A. S. B., Trammell S. R., 2002, ApJ, 574, 95
Stalevski M., Fritz J., Baes M., Nakos T., Popović L. C., 2012, MNRAS, 420, 2756
Suganuma M. et al., 2006, ApJ, 639, 46
Tinbergen J., 2006, Astronomical Polarimetry. Cambridge Univ. Press, Cambridge
Turner P. C., Forrest W. J., Pipher J. L., Shure M. A., 1992, ApJ, 393, 648
Urry C. M., Padovani P., 1995, PASP, 107, 803
Vrba F. J., Coyne G. V., Tapia S., 1981, ApJ, 243, 489
Wada K., 2012, ApJ, 758, 66
Wada K., Papadopoulos P. P., Spaans M., 2009, ApJ, 702, 63
Wardle J. F., Kronberg P. P., 1974, ApJ, 194, 249
Watanabe M., Nagata T., Sato S., Nakaya H., Hough J. H., 2003, ApJ, 591, 714
Weigelt G., Wittkowski M., Balega Y. Y., Beckert T., Duschl W. J., Hofmann K.-H., Men'shchikov A. B., Schertl D., 2004, A&A, 425, 77
Weinberger A. J., Neugebauer G., Matthews K., 1999, ApJ, 117, 2748
Whittet D. C. B., Martin P. G., Hough J. H., Rouse M. F., Bailey J. A., Axon D. J., 1992, ApJ, 386, 562
Woo J.-H., Urry C. M., 2002, ApJ, 579, 530
Young S., Hough J. H., Axon D. J., Bailey J. A., Ward M. J., 1995, MNRAS, 272, 513

This paper has been typeset from a TEX/LATEX file prepared by the author.